High threshold codes for neutral atom qubits with biased erasure errors

Kaavya Sahay,[1, 2, *] Junlan Jin,[3, *] Jahan Claes,[1, 2] Jeff D. Thompson,[3] and Shruti Puri[1, 2]

[1] *Yale University, Department of Applied Physics, New Haven, CT 06520, USA*

[2] *Yale Quantum Institute, Yale University, New Haven, Connecticut 06511, USA*

[3] *Princeton University, Department of Electrical and Computer Engineering, Princeton, NJ, 08544, USA*

(Dated: February 8, 2023)

The requirements for fault-tolerant quantum error correction can be simplified by leveraging structure in the noise of the underlying hardware. In this work, we identify a new type of structured noise motivated by neutral atom qubits, biased erasure errors, which arises when qubit errors are dominated by detectable leakage from only one of the computational states of the qubit. We study the performance of this model using gate-level simulations of the XZZX surface code. Using the predicted erasure fraction and bias of metastable ^{171}Yb qubits, we find a threshold of 8.2%, which is 1.9 times higher than the threshold for unbiased erasures, and 7.5 times higher than the threshold for depolarizing errors. Surprisingly, the improved threshold is achieved without bias-preserving controlled-not gates, and instead results from the lower noise entropy in this model. We also introduce an XZZX cluster state construction for measurement-based error correction, hybrid-fusion, that is optimized for this noise model. By combining fusion operations and deterministic entangling gates, this construction preserves the intrinsic symmetry of the XZZX code, leading to a higher threshold of 10.3% and enabling the use of rectangular codes with fewer qubits.

Quantum error correction (QEC) is essential to protect fragile quantum states during computation [1–3]. To achieve scalable quantum computation, the rate at which errors are introduced must be below a threshold error rate that depends on the noise model and error correction approach [4–7]. Recently, significant work has focused on identifying or engineering the structure of noise in qubits, which can lead to higher thresholds and reduced overhead if paired with appropriate gate operations and QEC architectures. For example, biased Pauli noise models can be engineered in superconducting cat qubits [8–10] and certain neutral atom qubits [11]. Given the availability of bias-preserving gates [12], this can lead to significantly improved thresholds and lower overhead for the XZZX surface code, which has special symmetries facilitating decoding this type of noise [13, 14]. Another example is qubits where errors can be converted with high probability into erasure errors. This model has been proposed for appropriately engineered qubit encodings and gates in neutral atoms [15], trapped ions [16] and superconducting qubits [17, 18], and leads to significantly increased thresholds [15–17, 19–21]

In this work, we identify a new error model, *biased erasure errors*, that arises when noise is dominated by erasures from only one computational state of the qubit. This model is physically motivated by metastable ^{171}Yb qubits, where erasures result from leakage out of the $|1\rangle$ computational state into levels whose population can be continuously monitored using cycling transitions that do not affect the qubit levels [15, 22]. We refer to this as a (Z-)biased erasure model, as detecting transitions outside the computational states reveals that the qubit was previously in $|1\rangle$, and can be represented as a Z error with 50% probability. The biased erasure model has more structure than the conventional erasure model,

where observing an erasure yields no information about the prior state of the qubit [15–17, 19–21, 23].

In this work, we study the performance of the biased erasure model in several contexts. We first consider the XZZX surface code with circuit-based syndrome extraction. We find a threshold of 8.2% when biased erasures comprise $R_e = 0.98$ of all gate errors, as predicted for ^{171}Yb under optimal conditions [15]. This is nearly double the threshold of 4.3% for a conventional erasure model, and approximately 8 times the threshold in a comparable depolarizing error model. Remarkably, this high threshold is obtained using only the native gate set of neutral atom qubits: single-qubit gates and controlled-Z (CZ) gates, but without bias-preserving controlled-not (CX) gates. We attribute the higher threshold to a lower noise entropy when erasures are biased compared to when they are not.

We also introduce a measurement-based QEC architecture, *hybrid-fusion*, that is specifically tailored for neutral atom qubits with biased erasure noise. This approach combines fusion operations with deterministic entangling gates to construct an XZZX cluster state that preserves the symmetry of the XZZX code under this biased noise, without requiring bias-preserving CX gates. In fusion-based (FB) error correction, an error correcting code is built by fusing together few-body entangled resource states using measurements of two-qubit Pauli operators $X \otimes X$ and $Z \otimes Z$. This method has been studied in linear optical quantum computing, where non-deterministic heralded fusions are the native entangling operation [24–28], and has the benefit of preserving the symmetry of the XZZX code when the fusion errors are biased [28]. We present a bias-preserving fusion circuit for neutral atom qubits, and combine this operation with deterministic entangling gates to develop a measurement-based error correction architecture with a high threshold, and reduced overhead and gate count. With this approach, we find an even higher threshold of

---

Model	$R_e = 0$	$R_e = 0.98$	$R_e = 1$	Preserves 2D symmetry?	Avoids atom replacement?
circuit, unbiased erasures	1.1%	4.3%	5.0%	N	N
circuit, biased erasures, native gates	1.1%	8.2%	10.3%	N	N
circuit, biased erasures, BCX	1.1%	9.0%	12.8%	Y	N
hybrid-fusion, native gates	1.0%	10.3%	14.7%†	Y	Y

TABLE I. Summary of thresholds derived in this work for the XZZX surface code under various error models and QEC architectures. Thresholds are obtained using an MWPM decoder, and are reported for several values of R_e. The first three rows give thresholds using circuit-based syndrome extraction (Sec. II), for unbiased erasures [15], and using the biased erasure model of Section I. The latter model is studied with and without bias-preserving CX gates, while the former case uses only the native gates (single-qubit gates and CZs) of the neutral atom platform. The last line is the hybrid-fusion error correction scheme introduced in Section III, with native gates. The final two columns indicate additional properties discussed in detail in Section IV: whether the dominant errors produce pairs of syndromes lying in 2D planes of the decoding graph (reducing qubit overhead in the limit of large bias), and whether mid-circuit atom replacement is necessary to recover from erasure errors. †This numerically simulated threshold increases to 17.7% when using an erasure decoder at large system sizes (see text).

10.3% for $R_e = 0.98$. We also discuss other potential advantages of this approach for neutral atoms including robustness against atom loss and relaxed requirements for erasure detection and atom replacement.

While this noise model is physically motivated by metastable ^{171}Yb qubits, it may also be engineered in other qubits with prevalent erasure errors such as metastable trapped-ion qubits [16] or superconducting qubits encoded in the $|g\rangle, |f\rangle$ levels of transmons [17]. The high thresholds and reduced requirements for bias-preserving gate operations may encourage the development of new qubits or encodings. Finally, this work may stimulate further development of fusion-based QEC architectures for neutral atoms.

The main results of our work are summarized in Table I. We introduce the biased erasure error model in section I, and study its behavior using circuit-based error correction in section II. In section III, we introduce the hybrid-fusion architecture and study its performance. We discuss further opportunities for optimization in section IV, and conclude in section V.

I. BIASED ERASURE ERRORS IN NEUTRAL ATOMS

To motivate the biased erasure model, we consider how it arises naturally in neutral atom qubits. In this platform, two-qubit gates implemented using the Rydberg blockade are the dominant source of errors [29–32]. The only fundamental effect limiting the fidelity of two-qubit gates is the finite lifetime of the Rydberg state that is populated transiently during the gate [33]. In the particular case of ^{171}Yb [31, 34], encoding the qubit in the nuclear spin sublevels of the metastable $^3P_0$ scheme has the property that the majority of the decay events populate disjoint subspaces that can be detected efficiently, which converts these errors into erasure errors [15, 22]. Recent additional work has derived gate protocols to convert other errors such as quasi-static

laser noise and Doppler shifts into erasure errors through a similar mechanism [35, 36].

In this work, we consider an additional property of the physical error model of metastable ^{171}Yb qubits, which is that excitation to the Rydberg state $|r\rangle$ only occurs from the qubit state $|1\rangle$, and never from $|0\rangle$ [Fig. 1(a)] [11]. To illustrate the behavior of this model, consider a hypothetical single qubit operation involving excitation from $|1\rangle$ to $|r\rangle$, where the only possible error is a decay from $|r\rangle$ to a detectable, disjoint state $|e\rangle$. In the absence of an error, the qubit is coherently de-excited back to $|1\rangle$ at the end of the gate. This results in a quantum channel with Kraus operators:

$$K_0 = |0\rangle \langle 0| + \sqrt{1 - 2p_e} |1\rangle \langle 1| + |e\rangle \langle e| \qquad (1)$$

$$K_e = \sqrt{2p_e} |e\rangle \langle 1| \qquad (2)$$

The probability of an error, averaged over both computational states, is p_e.

Upon detection of an atom in $|e\rangle$, the qubit is reinitialized into $|1\rangle$, or replaced by a new qubit in $|1\rangle$, described by the recovery operator $\hat{R} = |1\rangle \langle e|$. The combined channel can be expressed by the Kraus operators:

$$W_0 = |0\rangle \langle 0| + \sqrt{1 - 2p_e} |1\rangle \langle 1| \qquad (3)$$

$$W_e = \hat{R} K_e = \sqrt{2p_e} |1\rangle \langle 1| \qquad (4)$$

We obtain an effective Pauli channel using the identity $|1\rangle \langle 1| = (I + Z)/2$ and the Pauli twirl approximation (PTA), which may be achieved in practice by inserting random single-qubit Pauli gates after atom replacement [37–39]. The portion of the channel describing the erasure error is:

$$W_e \rho W_e^{\dagger} = \frac{p_e}{2} (I\rho I + Z\rho Z) \qquad (5)$$

Since the resulting state has at most a Z error, we refer to this as a *biased erasure* error model.

To model a two-qubit CZ gate, we incorporate two additional considerations. First, the leakage of one atom
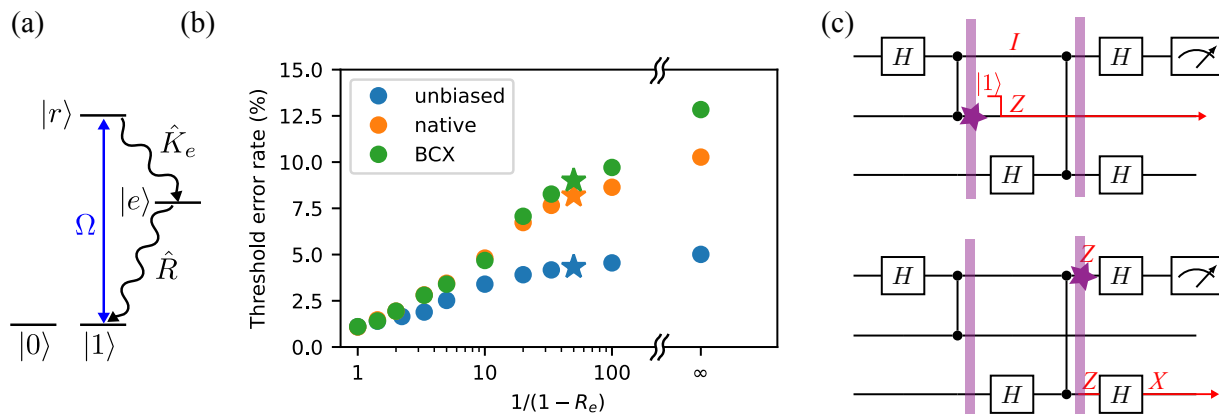
Figure 1. (a) Biased erasures arise when erasures (leakage to a detectable state $|e\rangle$) occur from only one qubit state, $|1\rangle$, such that recovery by replacement or reinitialization in the same state results in at most a Z error. (b) Threshold error rates as a function of R_e, under different error models: unbiased erasures (blue), biased erasures with native gates (orange) and biased erasures with bias-preserving CX (BCX) gates (green). The stars denotes $R_e = 0.98$. (c) Illustrative circuit measuring the two-qubit stabilizer ZX using native gates. When an erasure is detected during a two-qubit gate (purple star, depicting fluorescence detection of an atom in $|e\rangle$), the affected atom is replaced in $|1\rangle$ and the resulting state is described by an error drawn from $\{I, Z\}^{\otimes 2}$, but the manner in which this error propagates depends on its space-time location in the circuit. If the error occurs during the Z measurement (top), it propagates to the end of the circuit as a Z error. If the error occurs during the X measurement (bottom), it propagates to the end of the circuit as an X error. Knowledge of the error location makes this information available to the decoder, lowering the entropy of the noise.

can result in a dephasing error on the other atom as well [40]. Therefore, a two-qubit gate with an average erasure probability p_e is modeled by drawing an operator from the set $\{I, Z\}^{\otimes 2}$ with uniform probability $p_e/4$. Second, there is also a finite rate of non-erasure errors such as decays from $|r\rangle$ back to the qubit subspace. We model these as depolarizing errors with total rate p_p by drawing an operator from the set $\{I, X, Y, Z\}^{\otimes 2} \backslash \{I \otimes I\}$ with uniform probability $p_p/15$. The relative probability of these errors is given by the branching ratio $R = p_e/(p_e + p_p)$, which depends on the underlying physics of the qubit. For metastable ^{171}Yb, we have predicted $R = 0.98$ [15].

In this work, we only consider errors during two-qubit gates, which are by far the dominant errors for neutral atoms. A discussion of the role of measurement, single-qubit gate and idling errors on the unbiased erasure model can be found in Ref. [15].

Lastly, we note that the no-jump error also contributes a Z-biased Pauli error with probability Ap_e^2, because of the asymmetry in the erasure probability from the two qubit states [11, 15]. Continuing the previous example of a single-qubit gate, the evolution under the Kraus operator from Eq. (3) is:

$$ W_0 \rho W_0^\dagger \approx \left(1 - p_e - \frac{p_e^2}{4}\right) I \rho I + \frac{p_e^2}{4} Z \rho Z \qquad (6) $$

Here, we have applied the PTA and taken the limit $p_e \ll 1$.

We find $A = 1/4$ in Eq. (6), but for the two-qubit gate we estimate $A \approx 1/12$ [40]. We incorporate this by increasing the Pauli error probability to $p_p' = p_p + Ap_e^2$. In the resulting model, erasures constitute a fraction R_e

of all errors, with R_e given by:

$$ R_e = \frac{p_e}{p_p' + p_e} = \frac{R}{1 + AR^2(p_p + p_e)} \qquad (7) $$

To present a more generalizable model of biased erasures, we consider the error model to be defined by the independent parameters R_e and $p = p_p' + p_e$. Far below the threshold ($p \ll 1$), the behavior of ^{171}Yb can be estimated by setting $R_e = R = 0.98$. However, the performance near the threshold will be slightly different, since $R_e < R$. We note that $R_e = 1$ is not physically attainable for any value of R, but may be achievable in other physical models of biased erasure that act symmetrically on the qubit states.

II. CIRCUIT-BASED QEC WITH BIASED ERASURES

We quantify the advantage of the biased erasure model using circuit-level simulations of the XZZX code. The simulations use square codes with distance $d \leq 13$, implemented as d rounds of noisy stabilizer measurements followed by a final, noiseless stabilizer measurement [40]. The error syndromes are decoded using a minimum-weight perfect matching (MWPM) decoder, adjusting edge weights in each shot to incorporate the location of the erasure errors. The stabilizer simulations and construction of the decoding graph are implemented with Stim [41], while the decoding is implemented with Py-Matching [42]. Except where noted, the simulations do not consider bias-preserving CX gates. Therefore, CX gates are implemented using CZ gates, conjugated by

Hadamard (H) gates, which convert Z errors on the target qubit into X errors.

In Fig. 1(b), we show the threshold error rate p_{th} as a function of R_e. For comparison, we show three cases: unbiased erasures, biased erasures using only the native gates of the Rydberg platform, and biased erasures incorporating hypothetical bias-preserving CX gates.

For large values of R_e, biased erasures result in significantly higher thresholds than unbiased erasures, even in the absence of bias preserving gates. For example, at the value $R_e = 0.98$ projected for metastable ^{171}Yb qubits, the threshold is 8.2%, nearly twice the value with unbiased erasures ($p_{th} = 4.3\%$) and nearly eight times the threshold with depolarizing noise ($R_e = 0$, $p_{th} = 1.1\%$). The latter two thresholds are slightly higher than those reported in Ref. [15], because we use the slightly more accurate MWPM decoder, instead of a weighted Union Find decoder.

Previous works using the XZZX surface code to correct biased Pauli noise leverage its particular symmetry which guarantees that the pairs of error syndromes created by Z errors on the data and ancilla qubits lie in disconnected 2D planes [13, 14]. This advantage vanishes in the absence of bias-preserving gates (see, for instance, Ref. [8]). The fact that we observe high thresholds with only the native gates, and relatively little additional improvement from incorporating bias-preserving CX gates for $R_e < 1$ [Fig. 1(b)], suggests that another mechanism is responsible. This is reinforced by a separate calculation showing that the CSS and XZZX surface codes give almost the same threshold for biased erasures with native gates at $R_e = 0.98$.

We propose two alternate mechanisms for the high threshold with native gates. First, the biased erasure model has a lower error probability than the unbiased erasure model: given that an erasure has occurred, the biased model has an error with probability 3/4, while for the unbiased model, there is an error with probability 15/16. Second, even though Z errors can be converted into X errors in the absence of bias-preserving gates, erasure conversion after every gate allows this evolution to be tracked, lowering the entropy of noise [Fig. 1(c)] and reducing the impact of bias-preserving gates on the threshold.

Along with high thresholds, previous works on biased Pauli errors have also demonstrated reduced qubit overhead by using a thin rectangular XZZX code with the smaller distance for the low-rate error [8, 13]. For the biased erasure model, without bias-preserving CX gates, the dominant Z errors get converted to X errors. Thus, rectangular codes are not possible in the circuit-based approach. We will see in the next section that this can be overcome using a fusion-based approach to error correction.

For estimating the performance of biased erasure models in other qubit platforms that may have varying degrees of bias, and for including potential bias-degrading effects in ^{171}Yb, we have parameterized a finite bias version and computed thresholds as a function of bias in the supplementary information [40]. As in the case of biased Pauli noise [8, 13], we find that the rate of erasures from the low-probability state (here, $|0\rangle$) must be ~ 100 times less than the high-probability state to take full advantage of the bias.

III. HYBRID-FUSION QEC

Measurement-based error correction (MBEC) is an alternative approach to error correction based on performing local measurements on a many-body 3D entangled state called a fault-tolerant cluster state [43–47]. In the standard approach to realize a fault-tolerant cluster state, called *foliation*, one dimension of the cluster state effectively simulates time along which a planar encoded state is propagated via teleportation [48–51]. Indeed, the commonly used Raussendorf-Harrington-Goyal (RHG) or Raussendorf-Bravyi-Harrington cluster state [48, 49, 52] teleports the standard CSS surface code. Similarly, the recently introduced XZZX cluster state teleports the XZZX surface code [53].

To teleport a state from one planar array of qubits to the next, local destructive measurements are performed on the first array of qubits and measurement outcomes are recorded. After measurement, the first array of qubits can be re-intialized and reused to receive the encoded state from the second array. In this way, the entire 3D cluster state, with an arbitrary extent in the time-like direction, can be simulated by teleporting information back-and-forth between two planar surface code states. The measurement outcomes are subsequently processed to reconstruct the stabilizers and correct errors.

Fusion-based error correction (FBEC) is a particular approach for MBEC in which the cluster state is grown by fusing together few-body entangled resource states. Fusions are entangling operations carried out by performing destructive two-qubit measurements of $X \otimes X$ and $Z \otimes Z$. FBEC has been widely studied for linear optical quantum computing because fusions are the native entangling operations in that platform [24–28]. Recently, a fusion-based construction of the XZZX code was proposed that can maintain the symmetry of that code under biased noise if the fusion errors are biased [28].

In this section, we introduce a *hybrid-fusion* construction of the XZZX cluster state designed for metastable ^{171}Yb qubits with biased erasures that combines fusion operations and deterministic entangling gates. First, we design a bias-preserving fusion circuit that ensures that biased erasures in the physical gates only affect the $X \otimes X$ measurements, preserving $Z \otimes Z$. Then, we design a hybrid cluster state construction protocol that uses both fusions and direct CZ gates to entangle a collection of post-selected 8-qubit resource states (hereafter, *8-rings*). The operations and resource states are designed to minimize the number of CZ gates while ensuring that biased erasures at any step maintain the two-dimensional symmetry of the XZZX code. This simplifies the decoding problem, enabling higher thresholds
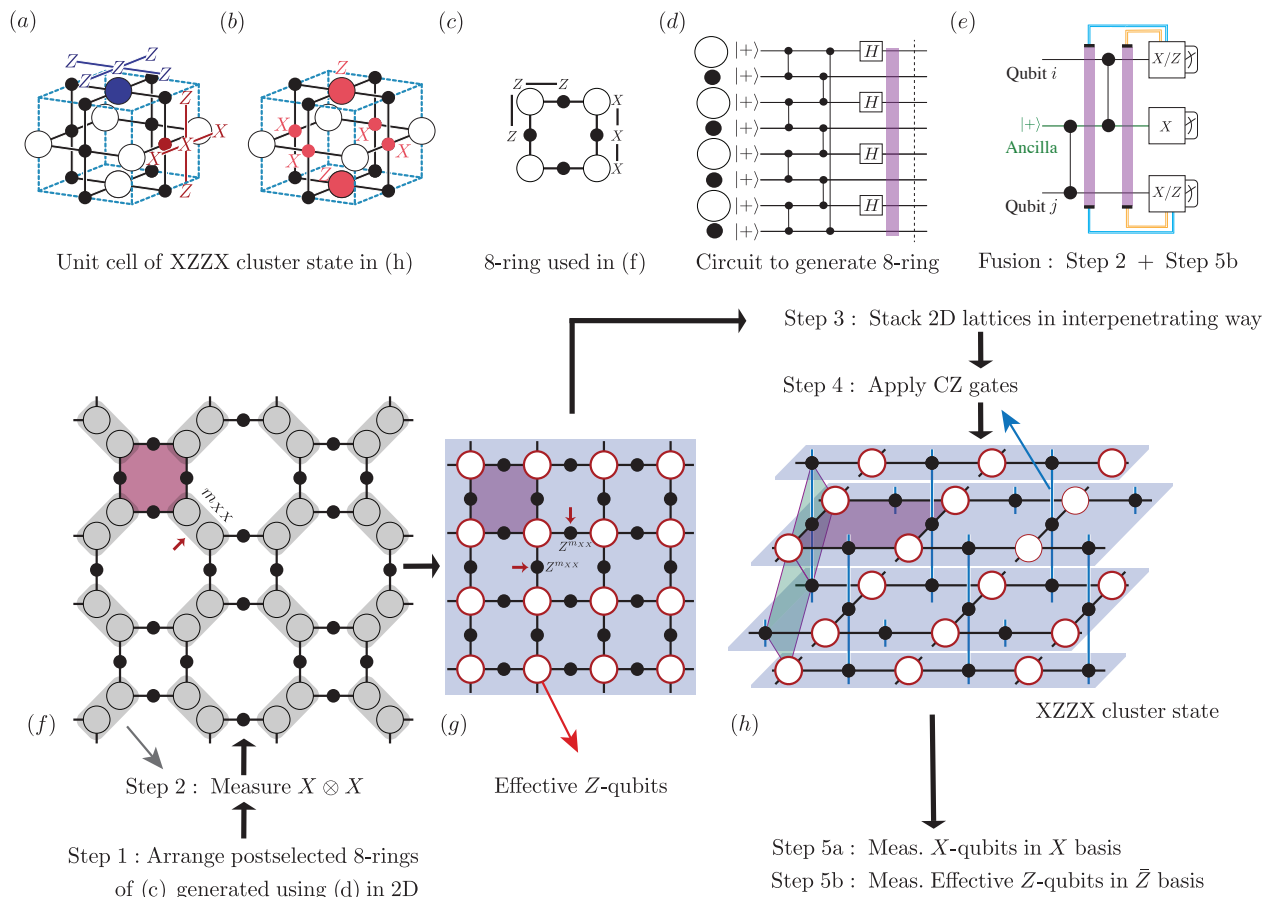
(a) (b) (c) (d) (e)

Unit cell of XZZX cluster state in (h)   8-ring used in (f)   Circuit to generate 8-ring   Fusion : Step 2 + Step 5b

Step 3 : Stack 2D lattices in interpenetrating way

Step 4 : Apply CZ gates

(f) (g) (h)

XZZX cluster state

Step 2 : Measure $X \otimes X$

Effective Z-qubits

Step 1 : Arrange postselected 8-rings
of (c) generated using (d) in 2D

Step 5a : Meas. X-qubits in X basis
Step 5b : Meas. Effective Z-qubits in $\bar{Z}$ basis

Figure 2. (a) A unit cell of the XZZX cluster state, with two examples of stabilizers centered on X (●)- and Z (○)- type qubits as described in the main text. (b) The cell stabilizer obtained by multiplying the stabilizers centered at all faces of a unit cell. (c) The 8-ring resource states used to build the cluster state. (d) Circuit to generate the resource state with ^{171}Yb atoms. The state is postselected on the absence of detected erasure errors. We have drawn only a single erasure detection step at the end of the circuit to reflect that the precise space-time location of the errors is not needed. In practice, a fluorescence detection is performed after every gate. (e) Circuit for adaptive, bias-preserving fusion measurements with ^{171}Yb atoms. Erasure detection (via fluorescence, purple lines) is performed following each gate. If any erasures occur, the measurement basis of the fusion qubits is changed from X to Z, ensuring that the value of $Z \otimes Z$ is preserved at the expense of $X \otimes X$. (f-h) Extended protocol for conceptual understanding of how the cluster state error correction is realized. For reference, in (h) we highlight in green a planar array of qubits encoded in XZZX surface code that is being propagated in time (left to right), generating the XZZX cluster state. Note that the entire cluster state shown does not need to be built at once, and can be realized using a small number of such planar arrays of qubits which are reused over time (see [40]).

and lower overhead [14, 28], which we demonstrate using circuit-level simulations.

A. The XZZX cluster state

The XZZX cluster state [53] is a stabilizer state defined on a graph with an X-*type* or Z-*type* qubit at each vertex, represented by ● and ○ respectively in Fig. 2(a). There is a stabilizer centered at each vertex. The stabilizer centered at a X-type qubit is the product of the Pauli X operator of that qubit, the Pauli Z operators of all adjacent X-type qubits and the Pauli X operators of all the adjacent Z-type qubits. The stabilizer centered at a Z-type qubit is the product of the Pauli Z

operator of that qubit and the Pauli Z operators of all adjacent X-type qubits. There is no edge between two Z-type qubits in the states considered here. Multiplying the stabilizers centered on the faces of a unit cell gives the six-body cell stabilizer, which is a product of Pauli X operators on the X-type qubits and Pauli Z operators on the Z-type qubits on the faces of the cell, as shown in Fig. 2(b). Measuring all Z-type qubits in the Z basis and all X-type qubits in the X basis teleports the XZZX surface code through this cluster state. To simultaneously perform error correction, the value of each cell stabilizer is constructed by adding the measurements outcomes of qubits around the faces of the unit cells.

In the XZZX cluster state, a Z error on an X-type qubit or an X error on a Z-type qubit causes its neigh-

boring cell stabilizers to flip [53]. Importantly, Z errors on X-type qubits only cause pairs of defects, or error syndromes, that are confined to lie in disconnected 2D layers, leading to more accurate decoding of errors and higher thresholds [13, 14, 53]. This feature reflects the symmetry that arises within the stabilizer group of the XZZX code under Z errors. Thus, to effectively use the XZZX cluster state to correct errors it is necessary to ensure that the dominant physical noise during cluster state preparation preserves this symmetry, that is, it only introduces Z errors on X-type qubits. We realize this goal using a combination of postselected resource states, bias-preserving fusions and CZ gates.

B. The resource state

The 8-ring resource state is defined by the graph in Fig. 2(c), and can be prepared using the circuit in Fig. 2(d). This circuit involves 8 CZ gates between neighboring X- and Z-type qubits on a ring. Biased erasures can result in unwanted X errors on Z-type qubits. However, postselecting completed rings on the absence of erasures allows these errors to be removed, while at the same time increasing the overall fidelity of the resource state. Using the notation of Section I, in the limit where $R_e \approx 1$ and $p_e \ll 1$, the success probability is $1 - 8p_e$ and the error probability of successful resource states is $\approx 8p'_p$. Many copies of this resource state can be prepared in parallel, and the successful ones can be moved into the positions for cluster state construction, described next, using movable optical tweezers [29, 54].

C. Adaptive, bias-preserving fusion measurements

Figure 2(e) presents an adaptive fusion measurement circuit with the property that biased erasures during two-qubit gates only cause an erasure of the $X \otimes X$ measurement outcome. In the ideal evolution without errors, the ancilla qubit measures $Z_i \otimes Z_j$ using CZ gates, followed by the single-qubit measurements $X_i \otimes I_j$ and $I_i \otimes X_j$, from which $X_i \otimes X_j$ can be computed [40].

In order to concentrate dominant errors into the $X_i \otimes X_j$ measurements and preserve the $Z_i \otimes Z_j$ information, we check for erasure errors in the two CZ gates, as shown in Fig. 2(e), and adapt the subsequent operations based on the location of these errors. In particular, when an erasure is detected, the protocol is aborted and each fusion qubit is measured independently in the Z basis with the measurement outcomes m_i (= 0 or 1) and m_j (= 0 or 1). The overall evolution is as if the atoms i, j were fused, with the $Z_i \otimes Z_j$ measurement outcome = $m_i \oplus m_j$, but the $X_i \otimes X_j$ measurement outcome is erased. We note that the Z measurement only needs to be performed on the fusion qubit that is not erased, because observing the erasure is equivalent to measuring the erased atom in $|1\rangle$. Therefore, the erased qubits also do not need to be replaced, unlike the approach in

Section II and Ref. [15].

D. Constructing the XZZX cluster state

Conceptually, the hybrid-fusion cluster state construction can be understood from the following steps. In *step 1* of the protocol, copies of postselected 8-ring resource states [Fig. 2(c)] are arranged in a plane as shown in Fig. 2(f). In *step 2*, an $X \otimes X$ measurement is performed on pairs of Z-type qubits at the neighboring corners. This measurement joins the pair of measured qubits into a single effective Z-type qubit with logical Z operator $\bar{Z} = Z \otimes Z$, giving a single 2D layer of the XZZX cluster state shown in Fig. 2(g) [26, 28]. To ensure that the post-measurement state is the stabilizer state defined by the graph in Fig. 2(g), a Pauli Z correction is applied to the two X-type qubits adjacent to one of the measured Z-type qubits conditional on the outcome of the $X \otimes X$ measurement [28]. In practice, this correction is tracked in software.

In *step 3*, copies of such 2D lattices are stacked on top of each other in a staggered manner such that the X-type qubits in one layer align with those in the next, while the Z-type qubits in one layer lie on top of a face in the next layer [Fig. 2(h)]. In *step 4*, a CZ gate is applied between each X-type qubit in layer k and another X-type qubit at the same location in layer $k + 1$ as shown in Fig. 2(h). This gives the entire 3D XZZX cluster state. Importantly, the CZ gates commute with each other and may be applied in any order. Here we follow a specific order: for each X-type qubit connected to unit cells to its left and right, the CZ gate with the X-type qubit in the layer above it is performed before the CZ gate with the layer below. If an erasure is detected in the first CZ gate, the second CZ gate is omitted to avoid introducing additional errors.

Now that we have the cluster state, we measure each qubit to teleport the XZZX surface code through the cluster state and to reconstruct the cell stabilizers of Fig. 2(b) for error correction. This is divided into two sub-steps. In *step 5a*, we measure each X-type qubit in X basis. In *step 5b*, we measure each effective Z-type qubits in the effective $\bar{Z}$-basis, by measuring $Z \otimes Z$ on the physical Z-type qubits composing the effective qubit.

We now observe that these operations can be regrouped to shorten the protocol. First, step 5b commutes with steps 5a, 4, 3, and 2, and can therefore be performed simultaneously with step 2. Steps 5b and 2 together constitute a fusion measurement, which removes Z-type qubits from the cluster state entirely. This fusion measurement is implemented using the circuit in Fig. 2(e). Furthermore, the staggered layer stacking and CZ gates in steps 3 and 4, respectively, can also be performed concurrently with or before the fusion measurements, as they act on a different subset of the qubits. Thus, the sequence of operations in the shortened protocol, summarized in Fig. 3, begins by preparing several copies of post-selected resource states and moving them
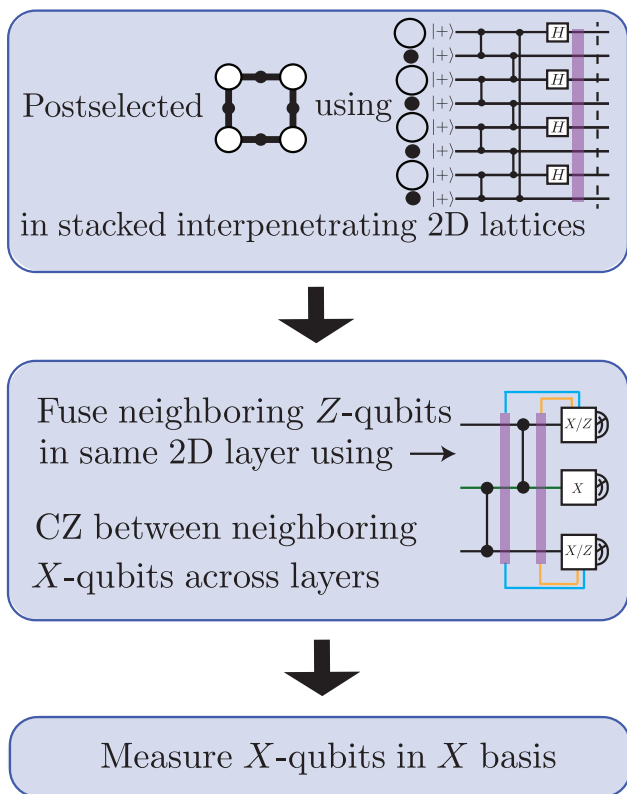
Figure 3. Proposed shortened protocol for high-threshold hybrid-fusion QEC with the XZZX cluster state using fusions and CZ gates.
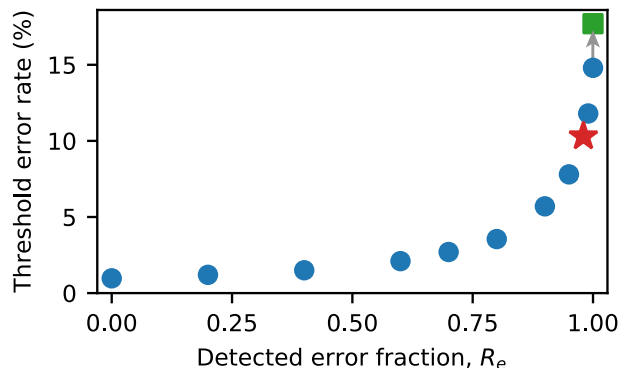

Figure 4. Threshold error rates for the hybrid-fusion architecture as a function of erasure fraction, R_e. The star denotes $R_e = 98\%$, while the green square marks the percolation threshold corresponding to the decoding graph for $R_e = 1$ (see text).

in position to form layers stacked in a staggered manner (steps 1,3), which is followed by fusions (steps 2, 5b) and CZ gates between layers (step 4), and finally measurement of X qubits in the X basis (step 5a).

E. Maintaining the XZZX code symmetry

Our hybrid-fusion approach is carefully designed to minimize the total number of CZ gates subject to the constraint of maintaining the symmetry of the XZZX code under biased erasures. To satisfy this constraint, we require that biased erasures only lead to Z errors on X-type qubits, but not to X errors on Z-type qubits. There are three types of entangling operations deployed in our approach: gates between X-type and Z-type qubits in the resource state [Fig. 2(d)], fusion operations [Fig. 2(e)], and gates between X-type qubits in adjacent layers [Fig. 2(h)].

Biased erasures in the resource state generation [Fig. 2(d)] do not maintain the system symmetry: Z errors arising from biased erasures in the CZ gates are converted into X errors on Z-type qubits by the Hadamard (effectively, Fig. 2(d) implements a non-bias-preserving CX between the Z-type and X-type qubits). However, we remove these errors from the cluster state by post-

selecting the resource states on the absence of erasures. The resource state is chosen such that no additional entangling gates between X- and Z-type qubits are needed after the post-selection step.

The second operation, fusion, uses adaptive measurements to maintain the error bias under biased erasures. Recall that the bias-preserving fusion circuit in Fig. 2(e) is designed to only erase the $X \otimes X$ measurement outcome. Since this result is used to apply a Z Pauli correction on the two adjacent X-type qubits [Fig. 2(g)], this results in a Z error on two X-type qubits in the cluster state, maintaining the desired symmetry.

The final operation, CZ gates joining the cluster state layers, has the desired behavior intrinsically: the CZ gates act only on X-type qubits, so the resulting biased erasures maintain the system symmetry.

The benefit of this approach can be understood by comparison to alternative cluster state constructions. Compared to directly entangling all the qubits in the cluster state, our hybrid-fusion approach results in the same number of biased erasure errors on the final cluster state, but ensures that they obey the 2D symmetry. However, the number of CZ gates, and thus the rough Pauli error rate on the final cluster state, is increased by a factor of 4/3. Therefore, our approach should outperform direct entanglement except when R_e is very small and Pauli errors are more important to correct than biased erasures. Compared to an all-fusion strategy like the 6-ring construction of Ref. [28], our strategy also has the same number of biased erasure errors on the final cluster state, but uses 2/3 the number of CZ gates. Therefore, our approach outperforms the all-fusion construction except when $R_e \gtrsim 0.99$, where the higher percolation threshold of the decoding graph in the all-fusion approach gives a slight advantage.

F. Threshold results

We evaluate the performance of our hybrid-fusion architecture under the biased erasure noise model by estimating the thresholds for different R_e (Fig. 4). Our simulations account for noise in the CZ gates used in the resource state generation circuit, the fusion circuit, and those of step 4, on a $d \times d \times d$ cluster state, with $d \leq 13$, which is equivalent to teleporting a $d \times d$ planar XZZX code while performing d rounds of stabilizer measurements in the circuit-based approach. Error syndromes are decoded using a MWPM decoder [55].

For $R_e = 1$ we achieve a threshold of 14.7% which is higher than that achieved with the circuit-based error correction. For $R_e = 0.98$, we obtain a threshold of 10.3%, higher than that achieved with the circuit-based approach with or without bias-preserving CX gates. In the other extreme of $R_e = 0$ when all source of noise is depolarizing Pauli noise, we obtain a threshold of 1%, similar to the threshold with circuit-based error correction at the same value of R_e.

Note that at $R_e = 1$, the threshold can also be determined from the bond-percolation threshold of the union-jack lattice and is expected to be $\sim 17.7\%$ [40]. The observed threshold in Fig. 4 is smaller than this because of finite size effects that are more prominent in the extreme case of $R_e = 1$ when the decoding graph is 2D. To confirm, we use a fast erasure decoder [56] to simulate extremely large lattices ($d \times d \times 5$ up to $d = 61$), and recover the threshold predicted by percolation theory in this limit. Since the erasure decoder and MWPM decoder achieve the same accuracy for erasure errors, we believe that we should achieve the same thresholds for both decoders at $R_e = 1$, but simulating such large lattices with MWPM is computationally prohibitive.

IV. DISCUSSION

We now make several comparisons between the presented circuit-based and hybrid-fusion approaches. Our hybrid-fusion protocol can be viewed as implementing QEC on a state encoded in a planar XZZX code as it is being teleported to another planar array of qubits. This is an alternative to using repeated rounds of quantum nondemolition stabilizer measurements as in conventional circuit-based error correction, but still allows transversal one- and two-qubit logical gate operations available for the planar surface code. In the supplementary material, we explicitly show how our hybrid-fusion protocol can be implemented with just a few planar arrays of qubits, starting and stopping with a 2D encoded XZZX surface code [40]. We note that neutral atoms are ideally suited to the high degree of connectivity required to implement hybrid-fusion: dynamic rearrangement of qubits is already used to postselect filled tweezer sites [57, 58], and coherent qubit transport has also been demonstrated [29, 54].

The hybrid-fusion approach has other advantages be-

yond the higher threshold, which we outline here but do not quantitatively analyze. As discussed, our construction preserves the system symmetry of the XZZX code under biased noise by ensuring that the high-probability Z erasures run along layers in Fig. 2(h). Thus, the same logical error rate can be achieved with fewer layers when R_e is large and the erasure are highly biased. This amounts to using a thin, rectangular XZZX surface code, which becomes a repetition code when $R_e = 1$ and the erasures are infinitely biased [13]. This allows for reduced overhead compared to the circuit-based approach, which requires a square XZZX code in the absence of bias-preserving gates. This property is summarized for each QEC architecture in Table I.

Second, the teleportation process converts lost atoms into Pauli errors, ensuring a finite threshold against loss errors or undetected erasures without additional leakage reduction units [59–63]. We leave an analysis of the threshold for a given loss rate to future work.

Finally, hybrid-fusion QEC relaxes the requirements for erasure detection and subsequent atom replacement. In the circuit-approach proposed in Ref. [15] and considered in Section II, the space-time location of each erasure error in the circuit must be resolved, and the affected qubits must be replaced or re-initialized as the computation proceeds. In the hybrid-fusion approach, this requirement is relaxed, in a way that is slightly different for the three steps involving two-qubit gates. For resource state preparation (step 1 of the protocol in Sec. III D), it is only necessary to determine if an erasure occurred at some point during the 8-ring preparation, and if it did, the entire state is discarded. Therefore, there is no need to replace affected qubits, and the necessary spatio-temporal resolution of the erasure detection is significantly coarser. During the fusion operations (steps 2, 5b), erasures must be detected immediately as the measurement basis is conditioned on this outcome, but the affected atoms do not need to be replaced. Finally, in the layer-joining CZ gates (step 4), atom replacement is not necessary, as the atoms are immediately measured. In summary, we find that conditionally replacing atoms at precise space-time locations is never required (as indicated in Table I), which may be a considerable experimental simplification.

V. CONCLUSION

To summarize, we have introduced a new noise model, biased erasure, that is physically motivated by metastable ^{171}Yb qubits but may also be engineered in other qubit platforms. We have studied two realistic QEC architectures under this noise model. The first is a circuit-based approach, where the improvement with the biased erasure model arises from the reduced entropy of this noise model, enabling more effective decoding. We obtain a threshold of 8.2% for the predicted metastable ^{171}Yb erasure fraction. The second is a hybrid-fusion approach with a systematic code con-

struction that gives rise to system symmetries under the biased erasure model. In this approach, we obtain a threshold of 10.3% for the metastable ^{171}Yb noise model. Compared to circuit-based syndrome extraction, this approach has the additional benefits of potentially enabling rectangular surface codes with lower overhead (in the limit of a large erasure fraction), robustness against atom loss, and simplified requirements for detecting and handling erasure errors in real-time.

There are several opportunities for further simplification and optimization of the hybrid-fusion approach for scalable fault-tolerant quantum computing. First, the threshold for hybrid-fusion QEC may be further improved by post-selecting on larger resource states [27]. This will decrease the rate of successfully generating the resource states, but it is still an experimentally viable route with deterministic, high-fidelity gates. For example, given a gate with 99.9% CZ fidelity, resource state chunks involving 100 CZ gates could be post-selected

with 90% success probability. Second, the hybrid-fusion approach naturally allows conversion of the planar surface code to a 3D surface code with transversal non-Clifford gates [64], which may lead to significant overhead reduction compared to alternative protocols for non-Clifford gates that rely on magic-state distillation.

VI. ACKNOWLEDGEMENTS

[1] Peter W. Shor, "Scheme for reducing decoherence in quantum computer memory," Phys. Rev. A **52**, R2493–R2496 (1995).

[2] P.W. Shor, "Fault-tolerant quantum computation," in Proceedings of 37th Conference on Foundations of Computer Science (1996) pp. 56–65.

[3] A. R. Calderbank and Peter W. Shor, "Good quantum error-correcting codes exist," Phys. Rev. A **54**, 1098–1105 (1996).

[4] Dorit Aharonov and Michael Ben-Or, "Fault-tolerant quantum computation with constant error," in Proceedings of the twenty-ninth annual ACM symposium on Theory of computing (1997) pp. 176–188.

[5] Emanuel Knill, Raymond Laflamme, and Wojciech H Zurek, "Resilient quantum computation," Science **279**, 342–345 (1998).

[6] Daniel Gottesman, "Theory of fault-tolerant quantum computation," Physical Review A **57**, 127 (1998).

[7] John Preskill, "Reliable quantum computers," Proceedings of the Royal Society of London. Series A: Mathematical, Physical and Engineering Sciences **454**, 385–410 (1998).

[8] Andrew S. Darmawan, Benjamin J. Brown, Arne L. Grimsmo, David K. Tuckett, and Shruti Puri, "Practical quantum error correction with the XZZX code and kerr-cat qubits," PRX Quantum **2**, 030345 (2021).

[9] Jérémie Guillaud and Mazyar Mirrahimi, "Repetition cat qubits for fault-tolerant quantum computation," Physical Review X **9**, 041053 (2019).

[10] Christopher Chamberland, Kyungjoo Noh, Patricio Arrangoiz-Arriola, Earl T Campbell, Connor T Hann, Joseph Iverson, Harald Putterman, Thomas C Bohdanowicz, Steven T Flammia, Andrew Keller, et al., "Building a fault-tolerant quantum computer using concatenated cat codes," PRX Quantum **3**, 010329 (2022).

[11] Iris Cong, Harry Levine, Alexander Keesling, Dolev Bluvstein, Sheng-Tao Wang, and Mikhail D. Lukin, "Hardware-efficient, fault-tolerant quantum computation with Rydberg atoms," Phys. Rev. X **12**, 021049 (2022).

[12] Shruti Puri, Lucas St-Jean, Jonathan A Gross, Alexander Grimm, Nicholas E Frattini, Pavithran S Iyer, Anirudh Krishna, Steven Touzard, Liang Jiang, Alexandre Blais, et al., "Bias-preserving gates with stabilized cat qubits," Sci. Adv. **6**, 5901 (2020).

[13] J Pablo Bonilla Ataides, David K Tuckett, Stephen D Bartlett, Steven T Flammia, and Benjamin J Brown, "The XZZX surface code," Nature communications **12**, 1–12 (2021).

[14] Benjamin J Brown, "Conservation laws and quantum error correction: towards a generalised matching decoder," arXiv preprint arXiv:2207.06428 (2022).

[15] Yue Wu, Shimon Kolkowitz, Shruti Puri, and Jeff D Thompson, "Erasure conversion for fault-tolerant quantum computing in alkaline earth Rydberg atom arrays," Nature Communication **13**, 4657 (2022).

[16] Mingyu Kang, Wesley C. Campbell, and Kenneth R. Brown, "Quantum error correction with metastable states of trapped ions using erasure conversion," arXiv preprint arXiv:2210.15024 (2022), 10.48550/ARXIV.2210.15024.

[17] Aleksander Kubica, Arbel Haim, Yotam Vaknin, Fernando Brandão, and Alex Retzker, "Erasure qubits: Overcoming the T_1 limit in superconducting circuits," arXiv preprint arXiv:2208.05461 (2022).

[18] James D Teoh, Patrick Winkel, Harshvardhan K Babla, Benjamin J Chapman, Jahan Claes, Stijn J de Graaf, John WO Garmon, William D Kalfus, Yao Lu, Aniket Maiti, et al., "Dual-rail encoding with superconducting cavities," arXiv preprint arXiv:2212.12077 (2022).

[19] Thomas M. Stace, Sean D. Barrett, and Andrew C. Doherty, "Thresholds for topological codes in the presence of loss," Phys. Rev. Lett. **102**, 200501 (2009).

[20] Sean D. Barrett and Thomas M. Stace, "Fault tolerant quantum computation with very high threshold for loss errors," Phys. Rev. Lett. **105**, 200502 (2010).

[21] Adam C. Whiteside and Austin G. Fowler, "Upper bound for loss in practical topological-cluster-state quantum computing," Phys. Rev. A **90**, 052316 (2014).

[22] Wesley C. Campbell, "Certified quantum gates," Phys. Rev. A **102**, 022426 (2020).

[23] M. Grassl, Th. Beth, and T. Pellizzari, "Codes for the quantum erasure channel," Phys. Rev. A **56**, 33–38 (1997).

[24] Daniel E. Browne and Terry Rudolph, "Resource-efficient linear optical quantum computation," Phys. Rev. Lett. **95**, 010501 (2005).

[25] Ying Li, Peter C. Humphreys, Gabriel J. Mendoza, and Simon C. Benjamin, "Resource costs for fault-tolerant linear optical quantum computing," Phys. Rev. X **5**, 041007 (2015).

[26] Sara Bartolucci, Patrick Birchall, Hector Bombin, Hugo Cable, Chris Dawson, Mercedes Gimeno-Segovia, Eric Johnston, Konrad Kieling, Naomi Nickerson, Mihir Pant, *et al.*, "Fusion-based quantum computation," arXiv preprint arXiv:2101.09310 (2021).

[27] Stefano Paesani and Benjamin J. Brown, "High-threshold quantum computing by fusing one-dimensional cluster states," arXiv preprint arXiv:2212.06775 (2022).

[28] Kaavya Sahay, Jahan Claes, and Shruti Puri, "Tailoring fusion-based error correction for high thresholds to biased fusion failures," arXiv preprint arXiv:2301.00019 (2022).

[29] Dolev Bluvstein, Harry Levine, Giulia Semeghini, Tout T. Wang, Sepehr Ebadi, Marcin Kalinowski, Alexander Keesling, Nishad Maskara, Hannes Pichler, Markus Greiner, Vladan Vuletić, and Mikhail D. Lukin, "A quantum processor based on coherent transport of entangled atom arrays," Nature **604**, 451–456 (2022).

[30] T. M. Graham, Y. Song, J. Scott, C. Poole, L. Phuttitarn, K. Jooya, P. Eichler, X. Jiang, A. Marra, B. Grinkemeyer, M. Kwon, M. Ebert, J. Cherek, M. T. Lichtman, M. Gillette, J. Gilbert, D. Bowman, T. Ballance, C. Campbell, E. D. Dahl, O. Crawford, N. S. Blunt, B. Rogers, T. Noel, and M. Saffman, "Multiqubit entanglement and algorithms on a neutral-atom quantum computer," Nature **604**, 457–462 (2022), number: 7906 Publisher: Nature Publishing Group.

[31] Shuo Ma, Alex P. Burgers, Genyue Liu, Jack Wilson, Bichen Zhang, and Jeff D. Thompson, "Universal gate operations on nuclear spin qubits in an optical tweezer array of ^{171}Yb atoms," Phys. Rev. X **12**, 021028 (2022).

[32] Nathan Schine, Aaron W. Young, William J. Eckner, Michael J. Martin, and Adam M. Kaufman, "Long-lived Bell states in an array of optical clock qubits," Nature Physics **18**, 1067–1073 (2022), number: 9 Publisher: Nature Publishing Group.

[33] Mark Saffman, T G Walker, and Klaus Mølmer, "Quantum information with Rydberg atoms," Reviews Of Modern Physics **82**, 2313–2363 (2010), publisher: American Physical Society.

[34] Alec Jenkins, Joanna W. Lis, Aruku Senoo, William F. McGrew, and Adam M. Kaufman, "Ytterbium Nuclear-Spin Qubits in an Optical Tweezer Array," Physical Review X **12**, 021027 (2022), publisher: American Physical Society.

[35] Sven Jandura, Jeff D Thompson, and Guido Pupillo, "Optimizing Rydberg gates for logical qubit performance," arXiv preprint arXiv:2210.06879 (2022).

[36] Charles Fromonteil, Dolev Bluvstein, and Hannes Pichler, "Protocols for Rydberg entangling gates featuring robustness against quasi-static errors," arXiv preprint arXiv:2210.08824 (2022).

[37] Emanuel Knill, "Quantum computing with realistically noisy devices," Nature **434**, 39–44 (2005).

[38] Lorenza Viola and Emanuel Knill, "Random decoupling schemes for quantum dynamical control and error suppression," Physical review letters **94**, 060502 (2005).

[39] Joel J Wallman and Joseph Emerson, "Noise tailoring for scalable quantum computation via randomized compiling," Physical Review A **94**, 052325 (2016).

[40] See Supplementary Material.

[41] Craig Gidney, "Stim: a fast stabilizer circuit simulator," Quantum **5**, 497 (2021).

[42] Oscar Higgott, "Pymatching: A python package for decoding quantum codes with minimum-weight perfect matching," ACM Transactions on Quantum Computing **3**, 1–16 (2022).

[43] Hans J. Briegel and Robert Raussendorf, "Persistent entanglement in arrays of interacting particles," Phys. Rev. Lett. **86**, 910–913 (2001).

[44] Robert Raussendorf and Hans J Briegel, "A one-way quantum computer," Physical Review Letters **86**, 5188 (2001).

[45] Robert Raussendorf, Daniel Browne, and Hans Briegel, "The one-way quantum computer–a non-network model of quantum computation," Journal of Modern Optics **49**, 1299–1306 (2002).

[46] Robert Raussendorf, Daniel E Browne, and Hans J Briegel, "Measurement-based quantum computation on cluster states," Physical Review A **68**, 022312 (2003).

[47] Hans J Briegel, David E Browne, Wolfgang Dür, Robert Raussendorf, and Maarten Van den Nest, "Measurement-based quantum computation," Nature Physics **5**, 19–26 (2009).

[48] Robert Raussendorf, Jim Harrington, and Kovid Goyal, "A fault-tolerant one-way quantum computer," Annals of Physics **321**, 2242–2270 (2006).

[49] Robert Raussendorf and Jim Harrington, "Fault-tolerant quantum computation with high threshold in two dimensions," Physical review letters **98**, 190504 (2007).

[50] A Bolt, G Duclos-Cianci, D Poulin, and TM Stace, "Foliated quantum error-correcting codes," Physical Review Letters **117**, 070501 (2016).

[51] Benjamin J Brown and Sam Roberts, "Universal fault-tolerant measurement-based quantum computation," Physical Review Research **2**, 033305 (2020).

[52] Robert Raussendorf, Sergey Bravyi, and Jim Harrington, "Long-range quantum entanglement in noisy cluster states," Physical Review A **71**, 062313 (2005).

[53] Jahan Claes, J Eli Bourassa, and Shruti Puri, "Tailored cluster states with high threshold under biased noise," npj Quantum Information **9**, 9 (2023).

[54] Jérôme Beugnon, Charles Tuchendler, Harold Marion, Alpha Gaëtan, Yevhen Miroshnychenko, Yvan R P Sortais, Andrew M Lance, Matthew P A Jones, Gaétan Messin, Antoine Browaeys, and Philippe Grangier, "Two-dimensional transport and transfer of a single atomic qubit in optical tweezers," Nature Physics **3**, 696–699 (2007), publisher: Nature Publishing Group.

[55] Vladimir Kolmogorov, "Blossom v: A new implementation of a minimum cost perfect matching algorithm," Mathematical Programming Computation **1**, 43–67 (2009).

[56] Nicolas Delfosse and Gilles Zémor, "Linear-time maximum likelihood decoding of surface codes over the quantum erasure channel," Physical Review Research **2**, 033042 (2020).

[57] Manuel Endres, Hannes Bernien, Alexander Keesling, Harry Levine, Eric R Anschuetz, Alexandre Krajenbrink, Crystal Senko, Vladan Vuletic, Markus Greiner, and Mikhail D Lukin, "Atom-by-atom assembly of defect-free one-dimensional cold atom arrays," Science **354**, 1024–1027 (2016), publisher: American Association for the Advancement of Science.

[58] Daniel Barredo, Sylvain de Léséluc, V Lienhard, T Lahaye, and A Browaeys, "An atom-by-atom assembler of defect-free arbitrary two-dimensional atomic arrays," Science **354**, 1021–1023 (2016), publisher: American Association for the Advancement of Science.

[59] Emanuel Knill, "Scalable quantum computing in the presence of large detected-error rates," Physical Review A **71**, 042322 (2005).

[60] Panos Aliferis and Barbara M Terhal, "Fault-tolerant quantum computation for local leakage faults," arXiv preprint quant-ph/0511065 (2005).

[61] Austin G Fowler, "Coping with qubit leakage in topological codes," Physical Review A **88**, 042308 (2013).

[62] Joydip Ghosh and Austin G Fowler, "Leakage-resilient approach to fault-tolerant quantum computing with superconducting elements," Physical Review A **91**, 020302 (2015).

[63] Martin Suchara, Andrew W Cross, and Jay M Gambetta, "Leakage suppression in the toric code," in *2015 IEEE International Symposium on Information Theory (ISIT)* (IEEE, 2015) pp. 1119–1123.

[64] Benjamin J Brown, "A fault-tolerant non-clifford gate for the surface code in two dimensions," Science Advances **6** (2020).

[65] Harry Levine, Alexander Keesling, Giulia Semeghini, Ahmed Omran, Tout T. Wang, Sepehr Ebadi, Hannes Bernien, Markus Greiner, Vladan Vuletić, Hannes Pichler, and Mikhail D. Lukin, "Parallel implementation of high-fidelity multiqubit gates with neutral atoms," Phys. Rev. Lett. **123**, 170503 (2019).

[66] Alec Jenkins, Joanna W. Lis, Aruku Senoo, William F. McGrew, and Adam M. Kaufman, "Ytterbium nuclear-spin qubits in an optical tweezer array," Phys. Rev. X **12**, 021027 (2022).

[67] M. Saffman, T. G. Walker, and K. Mølmer, "Quantum information with rydberg atoms," Rev. Mod. Phys. **82**, 2313–2363 (2010).

[68] Robert Parviainen, "Estimation of bond percolation thresholds on the archimedean lattices," Journal of Physics A: Mathematical and Theoretical **40**, 9253 (2007).

Supplementary Material: High threshold codes for neutral atom qubits with biased erasure errors

Kaavya Sahay,[1,2,*] Junlan Jin,[3,*] Jahan Claes,[1,2] Jeff D. Thompson,[3] and Shruti Puri[1,2]

[1] *Yale University, Department of Applied Physics, New Haven, CT 06520, USA*
[2] *Yale Quantum Institute, Yale University, New Haven, Connecticut 06511, USA*
[3] *Princeton University, Department of Electrical and Computer Engineering, Princeton, NJ, 08544, USA*
(Dated: February 8, 2023)

S1. ERROR CHANNEL

A. Two-qubit gate

Following the description of the single-qubit gate error channel in Section I in the main text, here we consider the more realistic two-qubit gate. Decay of one or both atoms to $|e\rangle$ can occur during the gate, which we approximate by the channel with Kraus operators:

$$K_0 = |00\rangle \langle 00| + \sqrt{1-p_1} (|10\rangle \langle 10| + |01\rangle \langle 01|) + \sqrt{1-p_2} |11\rangle \langle 11| + |e\rangle \langle e| \otimes I + I \otimes |e\rangle \langle e| + |ee\rangle \langle ee| \tag{S1a}$$

$$K_1 = \sqrt{p_1} |e0\rangle \langle 10| \tag{S1b}$$

$$K_2 = \sqrt{p_1} |0e\rangle \langle 01| \tag{S1c}$$

$$K_3 = \sqrt{p_2/3} |e1\rangle \langle 11| \tag{S1d}$$

$$K_4 = \sqrt{p_2/3} |1e\rangle \langle 11| \tag{S1e}$$

$$K_5 = \sqrt{p_2/3} |ee\rangle \langle 11| \tag{S1f}$$

Here, p_1 is the probability of decaying to $|e\rangle$ from the states $|01\rangle$ or $|10\rangle$, and p_2 is the probability for any decay to $|e\rangle$ from $|11\rangle$. For typical CZ gates, $p_1 \approx p_2$ because the Rydberg blockade results in only one atom in $|r\rangle$ in either case [15, 65]. The total erasure probability is defined by averaging over the computational states as $p_e = (2p_1 + p_2)/4$. After detecting whether any atoms are in $|e\rangle$, we apply one of the following recovery operators:

$$R_0 = I \tag{S2a}$$

$$R_1 = |1\rangle \langle e| \otimes I \tag{S2b}$$

$$R_2 = I \otimes |1\rangle \langle e| \tag{S2c}$$

$$R_3 = |11\rangle \langle ee| \tag{S2d}$$

This results in a channel with Kraus operators:

$$W_0 = R_0 K_0 = |00\rangle \langle 00| + \sqrt{1-p_1} (|10\rangle \langle 10| + |01\rangle \langle 01|) + \sqrt{1-p_2} |11\rangle \langle 11| \tag{S3a}$$

$$W_1 = R_1 K_1 = \sqrt{p_1} |10\rangle \langle 10| = \frac{\sqrt{p_1}}{4}(I+Z) \otimes (I-Z) \tag{S3b}$$

$$W_2 = R_2 K_2 = \sqrt{p_1} |01\rangle \langle 01| = \frac{\sqrt{p_1}}{4}(I-Z) \otimes (I+Z) \tag{S3c}$$

$$W_3 = R_1 K_3 = \sqrt{p_2/3} |11\rangle \langle 11| = \sqrt{\frac{p_2}{3}} \frac{1}{4}(I+Z) \otimes (I+Z) \tag{S3d}$$

$$W_4 = R_2 K_4 = W_3 \tag{S3e}$$
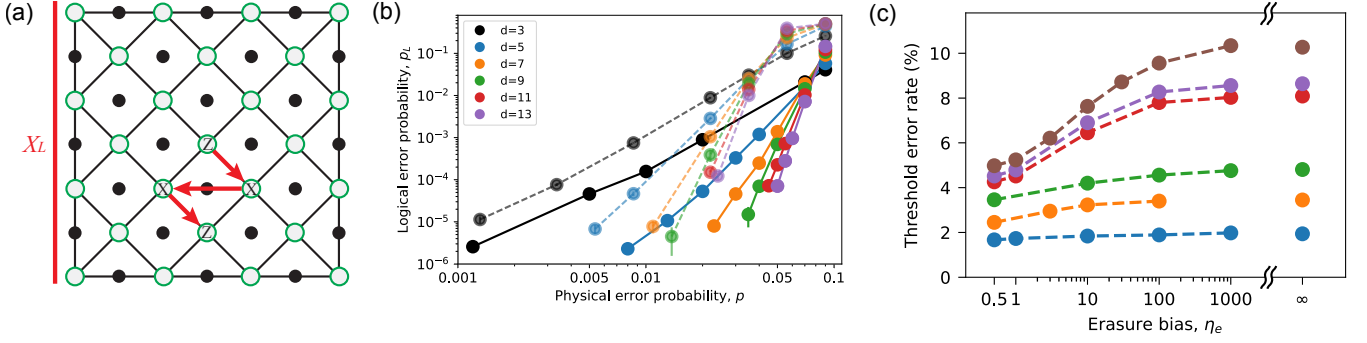
$$W_5 = R_3 K_5 = W_3 \tag{S3f}$$

Figure S1. (a) A patch of the XZZX surface code studied in this work, with the data and ancilla qubits denoted by the green open circles and black solid circles, respectively. The red arrows denote the sequence of the stabilizer measurement. (b) Scaling of the logical error rate with the physical error rate for code distances up to $d = 13$ with $R_e = 0.98$ in the case of unbiased erasure ($\eta_e = 1/2$, dashed lines) and fully biased erasure ($\eta_e = \infty$, solid lines). The threshold error rate increases from $p_{\text{th}} = 4.3\%$ to 8.1%. (c) Threshold error rates under different erasure bias for several R_e (from bottom to top, $R_e = 0.5, 0.8, 0.9, 0.98, 0.99, 1$). In all plots, the lines are a guide to the eye.

Applying the PTA as before yields the Pauli channel:

$$W_0 \rho W_0^\dagger \approx N II \rho II + \frac{p_2^2}{64} (IZ\rho IZ + ZI\rho ZI) + \frac{(2p_1 - p_2)^2}{64} ZZ\rho ZZ \tag{S4a}$$

$$W_1 \rho W_1^\dagger = W_2 \rho W_2^\dagger \approx \frac{p_1}{16} (II\rho II + IZ\rho IZ + ZI\rho ZI + ZZ\rho ZZ) \tag{S4b}$$

$$W_3 \rho W_3^\dagger = W_4 \rho W_4^\dagger = W_5 \rho W_5^\dagger \approx \frac{p_2/3}{16} (II\rho II + IZ\rho IZ + ZI\rho ZI + ZZ\rho ZZ) \tag{S4c}$$

where N is a normalization factor. The resulting qubit state is the same in all of the channels corresponding to an erasure detection ($i \geq 1$). Therefore, we group them together and consider their sum:

$$\sum_{i \geq 1} W_i \rho W_i^\dagger = \frac{p_e}{4} (II\rho II + IZ\rho IZ + ZI\rho ZI + ZZ\rho ZZ) \tag{S5}$$

which is the error model described in the main text.

The no-jump error when no erasure is detected is slightly more complicated than in the single qubit case presented in Sec. I. The physical interpretation of this error is that the absence of a detected error reveals information about the state, specifically, that it is less likely to be in a state from which it could have jumped to $|e\rangle$.

We note that the last coefficient in Eq. (S4a) would vanish when the two qubits jump independently ($p_2 = 2p_1$), indicating no correlated errors up to the second order. If $p_2 < 2p_1$ (which is the case in practice, because of the Rydberg blockade), then the extra weight of the ZZ term in Eq. (S4a) represents a correlated error, but we do not consider this aspect further since these errors are already very small below threshold. Using the definition of p_e and Eq. (S4a) with $p_1 = p_2$, we arrive at the estimated no-jump Pauli error contribution of $p_e^2/12$ that is referenced in Sec. I.

B. Erasures with finite bias

The analysis above describes infinitely biased erasures arising from the decay of the Rydberg state. However, other mechanisms can also give rise to erasure errors that need to be considered separately.

First, Refs. [35, 36] derived gate protocols that convert Doppler shifts and slow amplitude noise into leakage into the Rydberg state, which can be detected as an erasure error. Since only atoms in $|1\rangle$ are coupled into the Rydberg state in these protocols, as well, the erasure errors should also be strongly biased.

Second, decays out of the qubit subspace $^3P_0$ from Raman scattering from the dipole trap or the finite lifetime of this state also become erasures [15]. However, these are equally likely to occur from either qubit state, and are therefore better represented as unbiased erasures. Most likely, the same description applies to single-qubit rotations driven by Raman transitions, as in Ref. [66].

Finally, erasures in the CZ gates themselves are not infinitely biased if there is a finite probability to excite to (and decay from) the Rydberg state from $|0\rangle$. While this is strongly suppressed in typical hyperfine qubits in alkali atoms because of the large splitting associated with the ground state hyperfine coupling ($\approx 6.8\,\mathrm{GHz}$ in Rb) [67], it is a more significant effect in nuclear spin qubits in alkaline earth atoms because of the smaller splittings. In $^{171}\mathrm{Yb}$, the excitation probability of $|0\rangle$ is suppressed by the Zeeman splitting in the Rydberg state [31]. For the $^3S_1$ state, the average occupation of the Rydberg state during a gate when starting from $|0\rangle$ is approximately $p_0 = (\hbar\Omega)^2/(g_F\mu_B B)^2$, with $g_F = 4/3$. For reasonable values of $\Omega \approx 5\,\mathrm{MHz}$, p_0 can be suppressed below 10^{-3} in a magnetic field over 100 Gauss.

To incorporate these effects, we introduce the following phenomenological model. When an erasure error occurs during a CZ gate (with probability p_e), the state of each atom after recovery is modeled by selecting a Pauli operator from $\{I, Z\}$ with probability $p_I = p_Z \equiv p_a$, or from $\{X, Y\}$ with probability $p_X = p_Y \equiv p_b$, where $2(p_a + p_b) = 1$. Defining the erasure bias $\eta_e = p_a/2p_b$, we arrive at the thresholds summarized in Fig. S1(c). In the experimentally relevant range of R_e, we see significant improvement in the threshold already for $\eta_e = 10$, with saturation effects visible above $\eta_e = 100$.

S2. CIRCUIT-BASED QEC

Here we describe in more detail the circuit-level simulation of the XZZX surface code. We use a square unrotated XZZX lattice with a code distance d [see Fig. S1(a) for an example of $d = 4$]. In *step 1*, we initialize all qubits in $|+\rangle$ and then do a round of noiseless stabilizer measurement to initialize the logical-qubit. In *step 2*, we implement d rounds of noisy stabilizer measurement, considering only errors on two-qubit gates. We flip a coin after every two-qubit gate to include an erasure with probability $p_e = pR_e$. If an erasure does not occur, a Pauli error is introduced with probability $p_p = p(1 - R_e)$. In *step 3*, we do a round of noiseless stabilizer measurement, which can be considered as corresponding to readout of the logical-qubit state. The threshold is determined from the intersection of the curves of the logical error rate versus physical error rate for two code distances $d = 9, 13$.

We study three different error models: (i) unbiased erasure, (ii) biased erasure with native gates, and (iii) biased erasure with bias-preserving CX gates. In case (i), if an erasure occurs, errors are drawn uniformly at random from $\{I, X, Y, Z\}^{\otimes 2}$. In case (ii), for infinitely biased erasure, errors arising from erasures during CZ gates are drawn uniformly at random from $\{I, Z\}^{\otimes 2}$. Errors from CX gates are drawn from $\{I, Z\} \otimes \{I, X\}$, since CX gates are implemented using CZ gates conjugated by H gates on the target qubit.

Following the discussion in Sec. S1 B, when considering erasure with finite bias η, the error from a CZ gate is simulated by letting the two qubits experience $\{I, Z, X, Y\}$ with probabilities $p_I = p_Z = \eta/(1 + 2\eta)$ and $p_X = p_Y = 0.5/(1 + 2\eta)$. In case (iii), for infinitely biased erasure, errors from both CZ and CX gates are drawn uniformly at random from $\{I, Z\}^{\otimes 2}$. In all cases, the remaining Pauli errors (not arising from erasures) are assumed to be depolarizing, i.e., drawn uniformly at random from $\{I, X, Y, Z\}^{\otimes 2} \backslash \{I \otimes I\}$.

We note that since all qubits start in $|+\rangle$ after the initialization in step 1, the logical qubit is in the $(+1)$ eigenstate of the logical X operator. Therefore, the derived logical error rate is effectively the logical Z error rate. One can also start with all qubits in state $|1\rangle$ instead of $|+\rangle$ to get the logical X error rate, and evaluate separate thresholds for logical Pauli-X and Pauli-Z errors (similar to Ref. [13]). In cases (i) and (ii), the two thresholds should be the same since the probabilities of X and Z errors on individual data qubits are equal. This is consistent with our simulations. In case (iii), since Z errors dominate X errors on all qubits, we evaluate the threshold using the logical Z error rate (note that despite different error rates, the discrepancy between the two thresholds is small).

The probabilities in step 2 described above, following the model in [15], are used when deriving the threshold corresponding to $R_e = 0.98$ (predicted for $^{171}\mathrm{Yb}$ atom qubits) for comparison with the result in [15]. In other cases of the circuit-based QEC studied in this work, we obtain the thresholds with a slightly modified version of error introduction in step 2. When adding Pauli errors to a two-qubit gate that does not have an erasure, we change the error probability from p_p to $p_p/(1 - p_e)$ to represent conditioning on the absence of an erasure. The corresponding effect on the threshold is small as one can expect from $1 - p_e \approx 1$. For instance, for $R_e = 0.98$ listed in Table 1 in the main text, in the case of infinite erasure bias with native gates, the threshold changes from 8.2% to 8.1% with this adjustment. In the cases of unbiased erasure and infinite erasure bias with bias-preserving gates, the respective thresholds have negligible changes.

S3. FUSION CIRCUIT

Here we provide a more detailed discussion of the fusion circuit introduced in the main text. Consider two qubits (labelled i, j) which need to be fused and which may be entangled with other qubits (collectively labelled as R). We

cam write the state of this system as

$$|\psi\rangle = a\,|0\rangle_i\,|0\rangle_j\,|A\rangle_R + b\,|1\rangle_i\,|0\rangle_j\,|B\rangle + c\,|0\rangle_i\,|1\rangle_j\,|C\rangle_R + d\,|1\rangle_i\,|1\rangle_j\,|D\rangle_R \tag{S6}$$

with, $|a|^2 + |b|^2 + |c|^2 + |d|^2 = 1$. After fusion, i, j are unentangled from the rest of the system and a new state of R is created conditioned on the outcomes m_{XX} and m_{ZZ} of the $X \otimes X$ and $Z \otimes Z$ measurements respectively.

$$\begin{aligned}
|\psi\rangle_{R,m_{\mathrm{XX}}=0,m_{\mathrm{ZZ}}=0} &\propto a\,|A\rangle_R + d\,|D\rangle_R \\
|\psi\rangle_{R,m_{\mathrm{XX}}=1,m_{\mathrm{ZZ}}=0} &\propto a\,|A\rangle_R - d\,|D\rangle_R \\
|\psi\rangle_{R,m_{\mathrm{XX}}=0,m_{\mathrm{ZZ}}=1} &\propto b\,|B\rangle_R + c\,|C\rangle_R \\
|\psi\rangle_{R,m_{\mathrm{XX}}=1,m_{\mathrm{ZZ}}=1} &\propto b\,|B\rangle_R - c\,|C\rangle_R
\end{aligned} \tag{S7}$$

For convenience we have dropped the normalization constants from the above equations. We now explain how this transformation is achieved with the fusion circuit.

In the fusion circuit, a CZ gate is applied between each of the two fusion qubits and the ancilla. In the absence of erasures, which we refer to as *case 1*, the ancilla is measured in the X basis, which projects the fusion qubits in an eigenstate of $Z \otimes Z$ with eigenvalue given by the outcome of the ancilla measurement m_{a}. Thus after the ancilla measurement, the state $|\psi\rangle$ reduces to

$$\begin{aligned}
|\psi\rangle_{m_{\mathrm{ZZ}}=m_{\mathrm{a}}=0} &\propto a\,|0\rangle_i\,|0\rangle_j\,|A\rangle_R + d\,|1\rangle_i\,|1\rangle_j\,|D\rangle_R \\
|\psi\rangle_{m_{\mathrm{ZZ}}=m_{\mathrm{a}}=1} &\propto b\,|1\rangle_i\,|0\rangle_j\,|B\rangle_R + c\,|0\rangle_i\,|1\rangle_j\,|C\rangle_R
\end{aligned} \tag{S8}$$

Next we measure $X \otimes I$, $I \otimes X$ with measurement outcomes m_i, m_j respectively. After this the fusion qubits are unentangled from R the state of which is $|\psi\rangle_{R,m_{\mathrm{XX}}=m_i \oplus m_j, m_{\mathrm{ZZ}}=m_{\mathrm{a}}}$ as desired. Thus in the absence of errors, the circuit indeed performs the correct fusion operation.

Next we consider the situation when an erasure is detected. If only the ancilla is erased then each fusion qubit is measured independently in the Z basis with the measurement outcomes m_i', m_j'. This gives $m_{ZZ} = m_i' \oplus m_j'$. In the biased erasure model, the qubit can only be erased if it started from the $|1\rangle$ state. So if one of the fusion qubits is erased then it is effectively measured in the Z basis with measurement outcome 1. Thus, if only one of the fusion qubits is erased then we measure the other qubit in Z basis to obtain the outcome m, so that $m_{\mathrm{ZZ}} = m \oplus 1$. If both qubits are erased then we know that $m_{ZZ} = 0$.

S4. ERROR CORRECTION WITH PLANAR ARRAYS OF QUBITS

Figure S2(a) shows how a foliated repetition code can be implemented with just two linear chains of resource states. The repetition code is teleported back-and-forth between the qubits marked in blue. We start with a repetition code and bring in post-selected resource states. Next, we perform the fusions and single qubit X measurements on the two arrays marked with grey and red boxes respectively. This effectively measures all the stabilizers of the repetition code once and teleports the repetition code to the top blue row of qubits. This process can be repeated based on the desired number of rounds of error correction. A more qubit-efficient procedure is shown in Fig. S2(b). Here, we use only a single array of resource states at a given time, but the array needs to be reinitialized twice per-round of stabilizer measurement.

Figure S3 shows how the XZZX surface code can be implemented with just four planar arrays of resource states. The figure focuses on a single stabilizer plaquette for clarity. The code is teleported back-and-forth between the qubits marked in red and black placed at the corners of the plaquette. We start with the XZZX code and bring in post-selected resource states. Next, we perform the fusions and single qubit X measurements which effectively measure all the stabilizers of the XZZX code once and teleports it to a new plane on the right. This process can be repeated depending on the desired number of rounds of error correction. Just like for the repetition code, we can reduce the number of layers to two and trade space for time.

S5. DECODING GRAPH FOR HYBRID-FUSION CONSTRUCTION AT $R_e = 1$

Starting from 8-ring resource states, the cluster state is built using two primary operations: fusions within 2D planes, and CZ gates between planes. Biased erasures form the dominant error channel for both operations. In the following discussion we set $R_e = 1$, and so Pauli errors are absent and error syndromes are restricted to distinct two-dimensional planes.
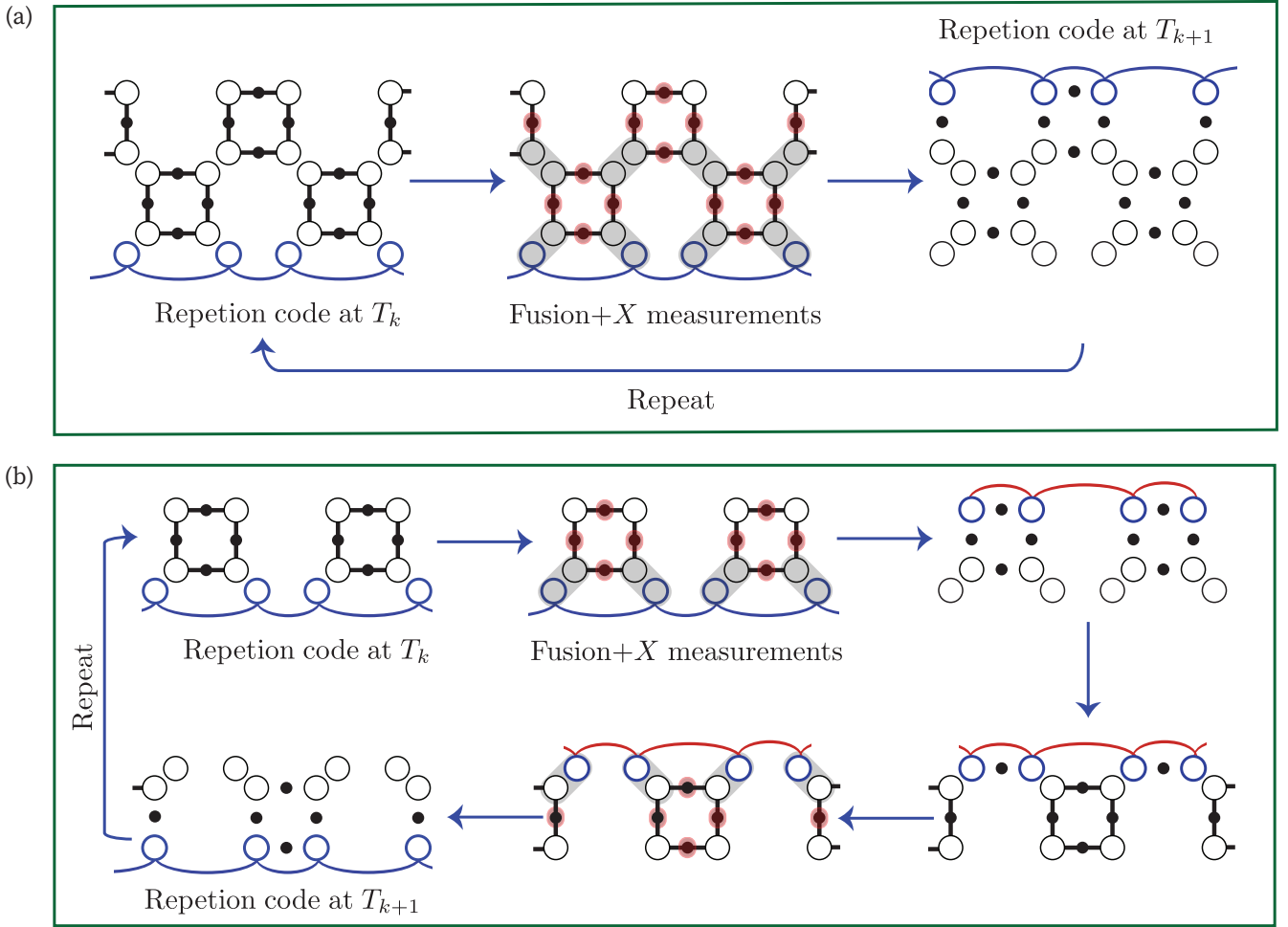
Figure S2. (a) Foliated repetition code implemented with just two linear chains of resource states. (b) Qubit-efficient implementation of the foliated repetition code. Space is traded off for time/number of steps it takes to measure one round of stabilizers.

Fusion failure on a Z-type qubit leads to a correlated $Z \otimes Z$ error on its two X-type neighbours in the resource state. This correlated error creates (-1) stabilizer outcomes in unit cells diagonally displaced from one another within this plane. An erasure during a CZ gate between two X-type qubits leads to a correlated Z error on both qubits. Since these two qubits create pairs of syndromes in unconnected planes, we consider these two errors independently. The resultant decoding graph is shown in Fig. S4, where the former resource states have been highlighted using dashed lines.

This graph is commonly referred to as the union-jack lattice, and is the dual of the $(4, 8^2)$ tiling of the plane. The percolation threshold p_{th} for this graph is naively 0.3232 [68], however, because errors from two gates contribute to every edge in the decoding graph, we have $2p_{th} - p_{th}^2 = 0.3232$, with the quadratic term appearing because we do not perform the second CZ gate on erasure detection at the first gate in both fusions and inter-layer CZs on qubits. Consequently, we obtain a theoretical threshold of $p_{th} = 17.7\%$ in terms of the error rate per gate. We recover this value by performing numerical simulations in the large-size limit.

XZZX surface code at T_k

Fusion+X measurements
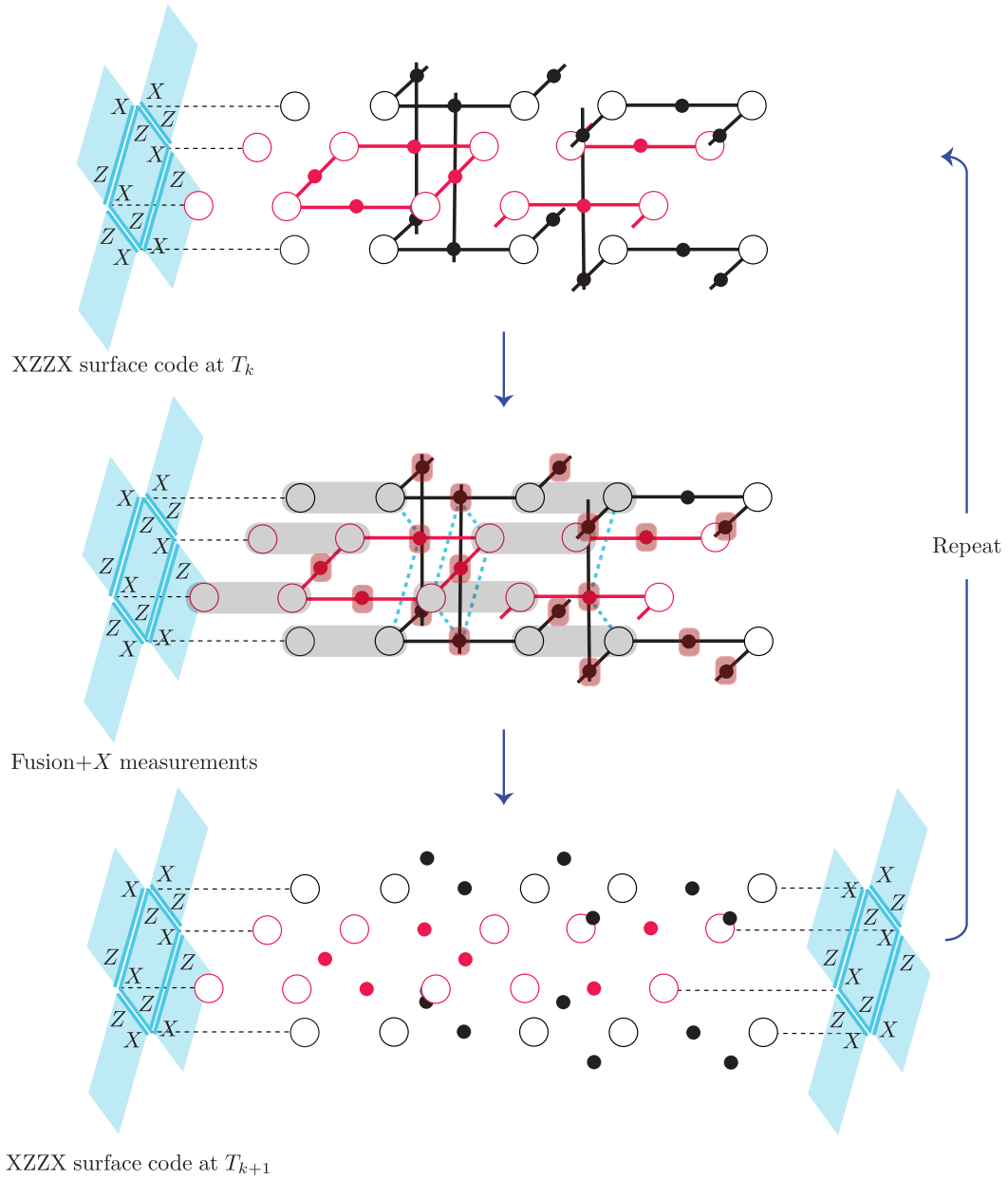
XZZX surface code at T_{k+1}

Repeat

Figure S3. XZZX cluster state implemented with just two planar layers of resource states
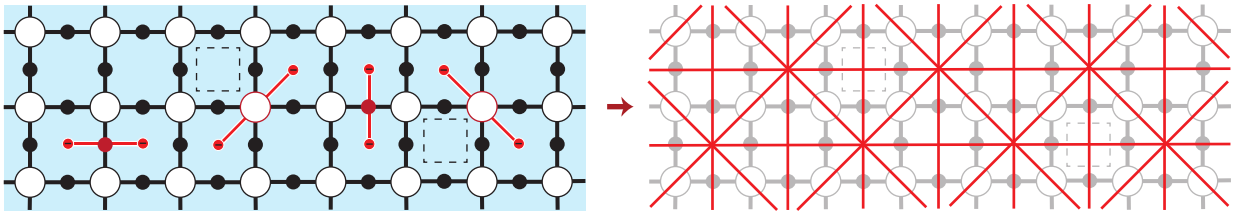

Figure S4. (left) Possible error syndromes arising from biased erasures during CZ gates and fusions between Z type qubits for a single plane of the XZZX cluster state. (right) The resultant syndrome graph used for decoding, highlighted in red, forms a union-jack lattice.